EPJ Nonlinear Biomedical Physics

Available online at:
http://www.epj-nbp.org

RESEARCH ARTICLE

OPEN ACCESS

Ionic Coulomb blockade and anomalous mole fraction effect in the NaChBac bacterial ion channel and its charge-varied mutants

Igor Kh. Kaufman[1,*], Olena A. Fedorenko[2], Dmitri G. Luchinsky[1,3], William A.T. Gibby[1], Stephen K. Roberts[2], Peter V.E. McClintock[1], and Robert S. Eisenberg[4]

[1] Department of Physics, Lancaster University, Lancaster LA1 4YB, UK
[2] Division of Biomedical and Life Sciences, Lancaster University, Lancaster, UK
[3] SGT, Inc., Greenbelt, MD 20770, USA
[4] Department of Molecular Biophysics, Rush University, Chicago, IL, USA

Abstract. Background. The selectivity of biological cation channels is defined by a short, narrow selectivity filter, having a negative net fixed charge Q_f. Voltage gated bacterial channels (NaChBac and some others) are frequently used in biophysics as simplified models of mammalian calcium and sodium channels. We report an experimental, analytic and numerical study of the effects of Q_f and bulk ionic concentrations of Ca^{2+} and Na^+ on conduction and selectivity of NaChBac channels, wild type and Q_f-varied mutants.
Methods. Site-directed mutagenesis and voltage clamp recordings were used to investigate the Na^+/Ca^{2+} selectivity, divalent blockade and anomalous mole fraction effect (AMFE) for different NaChBac wild type/ mutants channels and the properties dependence on Q_f. Experimental results were compared with Brownian dynamics simulations and with analytic predictions of the ionic Coulomb blockade (ICB) model, which was extended to encompass bulk concentration effects.
Results. It was shown that changing of Q_f from $-4e$ (for LESWAS wild type) to $-8e$ (for LEDWAS mutant) leads to strong divalent blockade of the Na^+ current by micromolar amounts of Ca^{2+} ions, similar to the effects seen in mammalian calcium channels. The BD simulations revealed a concentration-related logarithmic shift of the conduction bands. These results were shown to be consistent with ICB model predictions.
Conclusions. The extended ICB model explains the experimental (divalent blockade and AMFE) and simulated (multi-ion bands and their concentration-related shifts) selectivity phenomena of NaChBac channel and its charge-varied mutants. These results extend the understanding of ion channel selectivity and may also be applicable to biomimetic nanopores with charged walls.

Keywords: ionic Coulomb blockade / NaChBac / bacterial channel / electrostatic model / Brownian dynamics simulations / site-directed mutagenesis / patch-clamp technique

1 Introduction

Biological ion channels are natural nanopores providing for the fast and highly selective permeation of physiologically important ions (e.g., Na^+, K^+ and Ca^{2+}) through cellular membranes [1–3]. Despite its fundamental importance, and notwithstanding enormous efforts by numerous scientists, the physical origins of their selectivity still remain unclear. It is known, however, that the conduction and selectivity properties of cation channels are defined by the ions' movements and interactions inside a short, narrow selectivity filter (SF) lined by negatively charged amino acid residues that provide a net fixed charge Q_f [1,2].

NaChBac bacterial sodium channels [4–7] are frequently thought of, and used as, simplified experimental/ simulation models of mammalian calcium and sodium channels. X-ray investigations and molecular dynamics simulations have shown that these tetrameric channels possess strong binding sites with 4-glutamate {EEEE} loci at the SF [8]. Bacterial channels have been used in site-directed mutagenesis (SDM)/patch clamp studies of conductivity and selectivity [6,9].

Conduction and selectivity in calcium/sodium ion channels have recently been described [10–12] in terms of ionic Coulomb blockade (ICB) [13,14], a fundamental electrostatic phenomenon based on charge discreteness, an

* e-mail: i.kaufman@lancaster.ac.uk

electrostatic exclusion principle, and single-file stochastic ion motion through the channel. Earlier, Von Kitzing had revealed the staircase-like shape of the occupancy vs. site affinity for the charged ion channel [15] (following discussions and suggestions in [16]), and comparable low-barrier ion-exchange transitions had been discovered analytically [17]. A Fermi distribution of spherical ions was used as the foundation of a Poisson Fermi theory of correlated ions in channels [18,19].

ICB has recently been observed in sub-nm nanopores [14]. It appears to be closely similar to its electronic counterpart in quantum dots [20]. As we have demonstrated earlier [12], strong ICB appears for Ca^{2+} ions in model biological channels and manifests itself as an oscillation of the conductance as a function of Q_f, divalent blockade, and the anomalous mole fraction effect (AMFE) well-known for calcium channels [21].

Here, we present a combined experimental, analytical and numerical study of the influence of Q_f and the calcium concentration $[Ca]$ on the Ca^{2+}/Na^{+} selectivity of NaChBac channels/mutants. The investigation involved three complementary strands:
– an extension of the ICB model to encompass concentration-dependent effects;
– a numerical study the of the Ca^{2+}/Na^{+} selectivity and concentration-related occupancy shifts through Brownian dynamics simulations;
– an experimental study of the Ca^{2+}/Na^{+} permeability ratio and divalent blockade/AMFE in the bacterial sodium NaChBac channel and its mutants.

The main aim was to test ICB model predictions of the dependence on Q_f and $\log[Ca]$ of the conductivity type, and of the divalent blockade/AMFE properties. Site-directed mutagenesis and patch clamp measurements were used to investigate changes in the ion transport properties of the mutants caused by alterations in Q_f. Increasing the value of Q_f was expected to lead to stronger divalent blockade following the Langmuir isotherm and to a resonant variation of the divalent current with Q_f [12].

In what follows ε_0 is the permittivity of free space, e is the proton charge, z is the ionic valence, T the temperature and k_B is Boltzmann's constant.

2 Generic electrostatic model of calcium/ sodium ion channel

Figure 1 summarises the generic, self-consistent, electrostatic model of the selectivity filter of a calcium/sodium channel introduced earlier [11]. It consists of a negatively charged, axisymmetric, water-filled, cylindrical pore through the protein hub in the cellular membrane; and, we suppose it to be of radius $R = 0.3$ nm and length $L = 1.6$ nm [22], to match the dimensions of the selectivity filters of Na^{+}/Ca^{2+} channels.

There is a centrally placed, uniformly charged, rigid ring of negative charge $0 \le |Q_f/e| \le 10$ embedded in the wall at $R_Q = R$ to represent the charged protein residues of real Ca^{2+}/Na^{+} channels. The left-hand bath, modeling the extracellular space, contains non-zero concentrations of Ca^{2+} and/or Na^{+} ions. For the Brownian dynamics
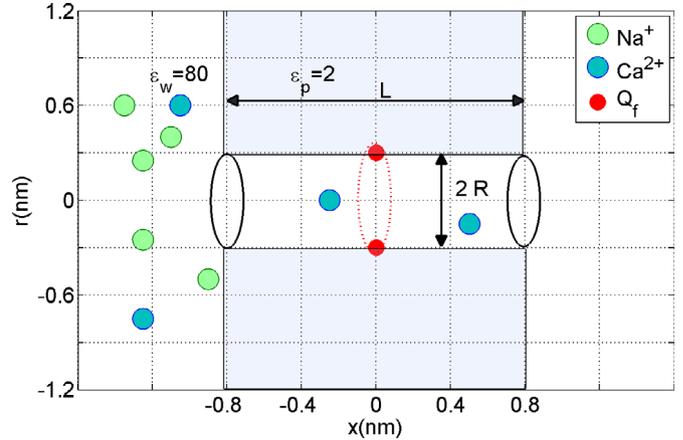
Fig. 1. Generic electrostatic model of calcium/sodium ion channel [11]. The model describes the channel's selectivity filter as an axisymmetric, water-filled pore of radius $R = 0.3$ nm and length $L = 1.6$ nm through a protein hub embedded in the cellular membrane. A centrally placed, uniform, rigid ring of negative charge Q_f is embedded in the wall to represent the charged residues of real Ca^{2+}/Na^{+} channels. We take both the water and the protein to be homogeneous continua describable by relative permittivities $\varepsilon_w = 80$ and $\varepsilon_p = 2$, respectively, together with an implicit model of ion hydration whose validity is discussed elsewhere. The moving monovalent Na^{+} and divalent Ca^{2+} ions are assumed to obey self-consistently both Poisson's electrostatic equation and the Langevin equation of motion.

simulations, we used a computational domain length of $L_d = 10$ nm and radius $R_d = 10$ nm, and grid size of $h = 0.05$ nm. A potential difference in the range 0–25 mV (corresponding to the depolarized membrane state) was applied between the left and right domain boundaries. We take both the water and the protein to be homogeneous continua describable by relative permittivities $\varepsilon_w = 80$ and $\varepsilon_p = 2$, respectively, together with an implicit model of ion hydration whose validity is discussed elsewhere [11]. These model parameters are assumed to be appropriate for the NaChBac channel, both for the wild type and for its mutants [23].

Of course, our reduced model represents a significant simplification of the actual electrostatics and dynamics of ions and water molecules within the narrow selectivity filter due to, for example: the application of continuum electrostatics; the use of the implicit solvent model; and the assumption of 1D (i.e., single-file) movement of ions inside the selectivity filter. The validity and range of applicability of this kind of model have been discussed in detail elsewhere [11,12,24].

3 Ionic Coulomb blockade and concentration-related shift

Coulomb blockade (whether ionic or electronic) arises in low-capacitance, discrete-state systems for which the ground state $\{n_G\}$ with n_G ions in the channel is separated
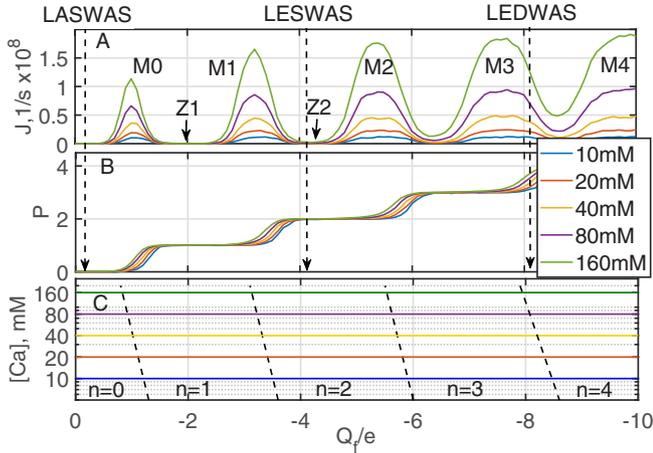
Fig. 2. Multi-ion Ca^{2+} conduction/occupancy bands in the model calcium/sodium channel, showing occupancy shifts with ionic concentration. (A) Strong multi-ion calcium conduction bands M_n as established by Brownian dynamics simulations. (B) The corresponding Coulomb staircase of occupancy P_c for different values of the extracellular calcium concentration $[Ca]$, as marked, consists of steps in occupancy that shift slightly as $[Ca]$ changes. The neutralized states Z_n providing blockade are interleaved with resonant states M_n. The vertical black-dashed lines show the nominal positions of the LESWAS and LEDWAS channel/mutants. (C) Coulomb blockade-based phase diagram. The positions of the $\{n\} \rightarrow \{n+1\}$ transitions (from Eq. (6)) are shown as sloping black-dashed lines. The horizontal coloured lines are guides to the eye, indicating the three concentrations used in the simulations. The diagram is consistent with the logarithmic $[Ca]$-related shift of steps in the Coulomb staircase shown in (B).

from neighbouring $\{n_G \pm 1\}$ states by a deep Coulomb gap $U_s \gg k_B T$, so that we can define the strength of the ICB as $S_{ICB} = U_s/(k_B T)$. The ICB phenomenon manifests itself as multi-ion oscillations (alternating conduction bands and stop bands) in the Ca^{2+} conductance and channel occupancy as functions of Q_f [10,12].

Figure 2 presents the results of Brownian dynamics simulation of Ca^{2+} conduction and occupancy over an extended range of Q_f ($0-10e$). Plot A shows strong oscillations of the conductance (conduction bands [10]); plot B shows the corresponding occupancy P, which forms a Coulomb staircase, as predicted by the ICB model [12]. Plot B also reveals concentration-related shifts of the staircase. Plot C contains a *phase-transition diagram* accounting for the observed shifts (see below).

Figure 3 presents a comparable set of Brownian dynamics results for the Na^+ conduction and occupancy. Plot A shows weaker conductance oscillations (conduction bands [10]); plot B shows the corresponding occupancy P, which forms a partly washed-out Coulomb staircase, as predicted by the ICB model [12]. Plot B also shows concentration-related shifts of the staircase.

We now present an extended ICB model to account for these concentration-related shifts, leading to the phase diagram of Figure 2C.

We define the positions of the resonant conduction points M_n (where barrier-less conduction can occur because $G_n = G_{n+1}$, where G_n is the Gibbs free energy when there
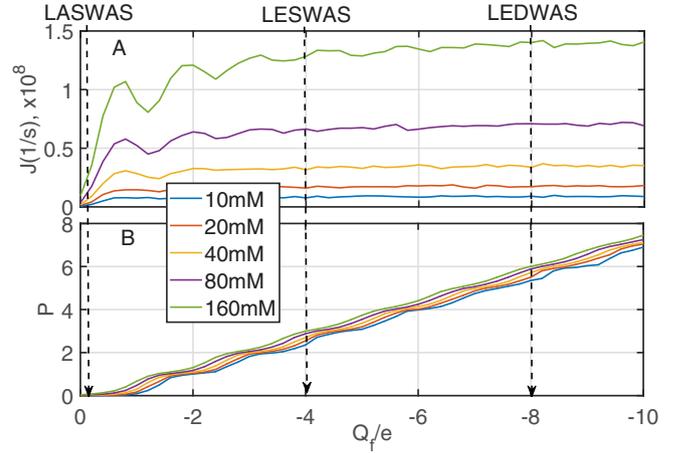
Fig. 3. Multi-ion Na^+ conduction/occupancy bands in the model calcium/sodium channel, showing occupancy shifts with ionic concentration. (A) Weak multi-ion sodium conduction bands M_n as established by Brownian dynamics simulations. (B) The corresponding occupancy P_c is an almost-washed-out Coulomb staircase whose steps shift slightly as the extracellular sodium concentration $[Na]$ changes. The vertical dashed lines show the nominal positions of the LESWAS channel and its LEDWAS mutant.

are n ions in the SF), taking account of bulk concentration and follow [12] in derivation. In equilibrium, the chemical potentials in the bulk μ_b and in the channels μ_c are equal, $\mu_b = \mu_c$ [25,26]:

$$\mu_b = \mu_{b,0} + k_B T \ln(P_b), \tag{1}$$

$$\mu_c = \mu_{c,0} + \Delta\mu_{c,ex}, \tag{2}$$

where the standard potentials $\mu_{b,0}$ and $\mu_{c,0}$ are assumed to be zero (although other choices are possible [12]), P_b stands for the equivalent bulk occupancy, related to the SF volume $V_{SF} = \pi R^2 L$, i.e., $P_b = n_b V_{SF}$, where n_b is bulk number density of the species of interest.

The excess chemical potential in the SF, $\Delta\mu_{c,ex}$, is defined here as the excess Gibbs free energy $\Delta G_n = \Delta U_n - T\Delta S_n$ in the SF due to the single-ion $\{n\} \rightarrow \{n+1\}$ transition. The SF entropy-related term $T\Delta S_n$ is model-dependent. We use the "single-vacancy" model of the motion [12,27] for which the following result can be derived [28]:

$$\Delta G_n = \Delta U_n + k_B T \ln(n+1). \tag{3}$$

Hence, the equilibrium ($\mu_b = \mu_c$) occupancy $P_c = \langle n \rangle$ around the transition point M_n represents a thermally rounded staircase (see Fig. 2B) described by a Fermi-Dirac distribution [12,17]:

$$P_c^* = P_c - n = \left[1 + \exp\left(\frac{\Delta G_n - \mu_b}{k_B T}\right)\right]^{-1}$$
$$= \left[1 + \frac{1}{P_b} \exp\left(\frac{\Delta G_n}{k_B T}\right)\right]^{-1}. \tag{4}$$
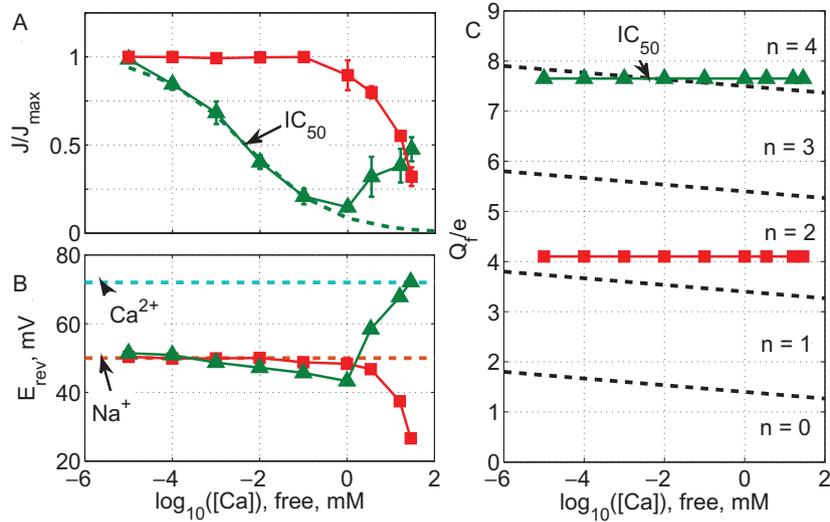
Fig. 4. Divalent blockade and anomalous mole fraction effect (AMFE) in wild-type NaChBac (LESWAS, shown as red squares) and LEDWAS (green triangles) mutant channels. Full lines are guides to the eye. The bath solution containing Na^+ and Ca^{2+} cations was adjusted by replacement of Na^+ with equimolar Ca^{2+}; the free Ca^{2+} concentrations $[Ca]$ are shown on the abscissa; and error bars represent the standard error in the mean (SEM). (A) Averaged normalized peak currents of LESWAS and LEDWAS channels. The Langmuir isotherm (9) fitted to the LEDWAS data for $[Ca] < 1$ mM is shown by the green dashed line. (B) Reversal potentials (E_{rev}) obtained from the same recordings as in A indicate that LEDWAS stopped conducting Na^+ if $[Ca^{2+}] \geq 1$ mM. Dashed lines indicate reference values when extracellular $[Ca^{2+}]$ (green) and $[Na^+]$ (red) are fixed to 100 mM. (C) Cartoon phase diagram Q_f vs. $\log([Ca])$, where the switching lines predicted by equation (6) are dashed-black.

It corresponds to the Coulomb staircase, well-known in Coulomb blockade theory [20], which appears when varying either Q_f or $\log(P_b)$.

The resonant value M_n of Q_f for the $\{n\} \rightarrow \{n+1\}$ transition is defined from the condition $\Delta G_n - \mu_b = 0$ as:

$$M_n = M_n^{CB} + \Delta M_n^P;$$
$$M_n^{CB} = -ze\left[(n+1/2) + \tilde{C}_0 \ln(n+1)\right], \quad (5)$$

$$\Delta M_n^P = ze\tilde{C}_0 \ln(P_b); \quad C_0 = \frac{C_0 k_B T}{z^2 e^2}, \quad (6)$$

where M_n^{CB} is the nominal M_n value, and the concentration-related shift ΔM_n^P is proportional to the logarithm of the concentration and to the dimensionless self-capacitance $\tilde{C}_0$.

The BD simulations results (Figs. 2 and 3) are in reasonable agreement with the ICB model, though the Q_f values for the resonant points M_n differ from the exact predictions of equation (6). This is because of singular ion-ion interactions that are not taken account of in the ICB model, and because of possible electric field leaks due to the finite length of the SF. That difference can be taken into account via the concept of an "effective charge". Ion-ion interactions could also account for the broadening of the conduction bands with growth of Q_f.

4 Phase transition diagrams

Next, we introduce the notion of "phase transition diagrams" (similar to [29]) and use them to describe the concentration-related shifts seen in our earlier [10] and

new Brownian dynamics simulations (Fig. 2B) and the divalent blockade/AMFE in mutation experiments on the bacterial NaChBac channel that we report below.

The phase diagrams (Figs. 2C and 4C) represent the evolution of the channel state on a 2-D plot with occupation $\log(P_b)$ (or equivalently $\log([Ca])$ concentration) on the ordinate axis and Q_f/e on the abscissa or vice versa. The phase transition lines (black, dashed) separate the states of the SF having different integer occupancy numbers $\{n\}$.

Different cross-sections through the diagram reflect different experiments and simulations in the sense that we can choose to vary either the concentration (divalent blockade/AMFE experiments) or Q_f (patch clamp experiments on mutants).

Let us start from the concentration-related shift of the Coulomb staircase. Figure 2C shows the switching lines and AMFE trajectory (projection of the system evolution) in the Ca^{2+} ionic occupancy phase diagram [17] for the calcium/sodium channel while Figure 2B shows the small concentration-related shifts of the Coulomb staircase for occupancy P found in the Brownian dynamics simulations [10]. Equation (6) and the phase diagram provide a simple and transparent explanation of the simulation results. The origin of the shift lies in the logarithmic concentration dependence of ΔM_n in equation (6). Similar shifts were seen in earlier simulations [15].

5 Site directed mutagenesis/patch clamp studies of NaChBac channel

The SF of NaChBac is formed by 4 trans-membrane segments each containing the six-amino-acid sequence LESWAS (leucine/glutamic-acid/serine/tryptophan/

Table 1. Main properties of the wild type (LESWAS) and mutant (LASWAS and LEDWAS) NaChBac bacterial channels generated and used for the present patch-clamp study. Here Q_f stands for the nominal fixed charge at the selectivity filter and IC$_{50}$ is the $[Ca]$ threshold value providing 50% blockade of the Na$^+$ current. Qualitative properties (selectivity and AMFE) are marked as "+" where present and "−" where absent.

Channel	SF amino acid sequence	Nominal Q_f/e	Ca^{2+}/Na selectivity	Divalent blockade, AMFE
Zero-charge mutant	L**A**SWAS	0	−	−
NaChBac wild-type	L**E**SWAS	−4	+ (Na > Ca)	−
Added-charge mutant	LE**D**WAS	−8	+ (Ca > Na)	+ (IC$_{50} = 5\,\mu$M)

alanine/serine, respectively, corresponding to residues 190–195). This structure provides the highly conserved {EEEE} locus with a nominal $Q_f = -4e$ [4]. As summarised in Table 1, site-directed mutagenesis was used to generate two mutant channels in which the SF either has "deleted charge" $Q_f = 0$ (L**A**SWAS, in which the negatively charged glutamate E191 is replaced with electrically neutral alanine) or has "added charge" $Q_f = -8e$ (LE**D**WAS, in which the electrically neutral serine S192 is replaced by negatively charged aspartate D) [4].

The methods used for preparation of the NaChBc mutants, and for the electro-physiology measurements, are summarised in Appendix A.

Whole cell current–voltage data were collected by recording responses to a consecutive series of step pulses from a holding potential of −100 mV at intervals of 15 mV beginning at +95 mV. All experiments were conducted at room temperature.

Figure 5 shows the original current traces using bath solutions containing either Na$^+$ or Ca^{2+} as the charge carrying cation, illustrating the permeability to these ions of the wild type NaChBac (LESWAS) ion channel and its mutants (LASWAS and LEDWAS).

Zero-charge mutants ($Q_f = 0$) did not show any measurable current in either of the solutions, corresponding well with the Coulomb-blocked state expected/measured for an uncharged channel or nanopore [12,14].

Wild type (LESWAS) channels ($Q_f = -4e$) exhibited high Na$^+$ conductance in agreement with earlier observations [4,5] and with the ICB model which predicts relatively Q_f-independent Na$^+$ conduction due to the small valence $z = 1$ of Na$^+$ ions [11,31].

LEDWAS channels with nominal $Q_f = -8e$ were found to conduct both Na$^+$ and Ca^{2+} (Fig. 5A), a result that coincides with the expectations shown in Figures 2 and 3.

These results for LESWAS and LEDWAS channels are consistent with previous reports [4,6,32]. The LEDWAS mutant contains a doubly-charged ring {EEEE+DDDD} locus instead of the singly charged ring {EEEE} locus of LESWAS but it was shown earlier [10] that the conduction bands are insensitive to the spatial distribution of charge along the SF.

SDM-based experiments with mammalian (Nav1.1, Cav1.2) [33,34] and bacterial (NaChBac, NavAB) [4,6,7,32] channels all show a very similar picture, i.e., growth of the Ca^{2+}/Na$^+$ conductance ratio with increasing $|Q_f|$. This is in qualitative agreement with the Coulomb blockade model, which predicted conduction bands for divalent cations in these high-Q_f mutants.

6 Mutation-induced divalent blockade and AMFE

The special and sensitive case of Ca^{2+}/Na$^+$ selectivity involves the phenomenon of divalent blockade/AMFE, which can be detected in purpose-designed experiments where the channel conduction $I([Na], [Ca])/I([Na], [0])$ vs. $[Ca]$ concentration is measured for very low $[Ca]$, where $[Na]$ is the concentration of Na$^+$. For channels presenting AMFE (e.g. Ca^{2+} channels) the initial addition of tiny concentrations of Ca^{2+} (in the nM or μM range) leads to a sharp drop in conduction, almost to zero (i.e., divalent blockade), and increases again with further growth of $[Ca]$ to the mM range [33,34]. It is known from experiments that this second conduction regime in AMFE is provided by a selective Ca^{2+} current, constituting the normal working mode of the L-type calcium channel [33].

To investigate divalent blockade and AMFE, we performed experiments using bath solutions containing mixtures of Na$^+$ and Ca^{2+}, at different concentrations. Ca^{2+} was added to a bath solution containing 140 mM Na$^+$ to achieve free Ca^{2+} concentrations from 10 nM up to 1 mM, which were achieved by adding HEDTA (for concentrations from 1 mM to 10 μM) or EGTA (for concentrations ≤1 μM).

Figure 4A shows that the current through the "added charge" mutant channel, LEDWAS, was highly sensitive to the presence of Ca^{2+}, and fell rapidly with increasing $[Ca]$. It exhibited strong Ca^{2+} blockade of its Na$^+$ currents, i.e., the divalent blockade phenomenon [5,33]. The blockade shape is frequently fitted empirically with a Langmuir isotherm, similarly to the cases of blockade by dedicated channel blocker drugs [5].

A complete description of divalent blockade and AMFE should account for statistical and kinetic features of the multi-species solution inside the SF [18,28]. We use a simplified description based on the assumptions:

$$[Ca] \ll [Na]; \ \tau_{Ca} \gg \tau_{Na}; \ P_c([Ca]) + P_c([Na]) \leq 1, \quad (7)$$

where τ_{Ca} and τ_{Na} stand for the respective ionic binding times. Under these assumptions, the SF can be in two exclusive states: "open" ($P_c([Ca]) = 0$, $J_{[Na]}([Ca]) = J_{[Na]}(0)$); and "closed", blocked by Ca^{2+} ions ($P_c([Ca]) = 1$, $J_{[Na]}([Ca]) = 0$), and the states are shared in time. Hence due to the ergodic hypothesis the blockade of the Na$^+$ current reflects Ca^{2+} occupancy:

$$J_{Na}([Ca]) = J_{Na}(0)(1 - P_c(Ca)). \quad (8)$$
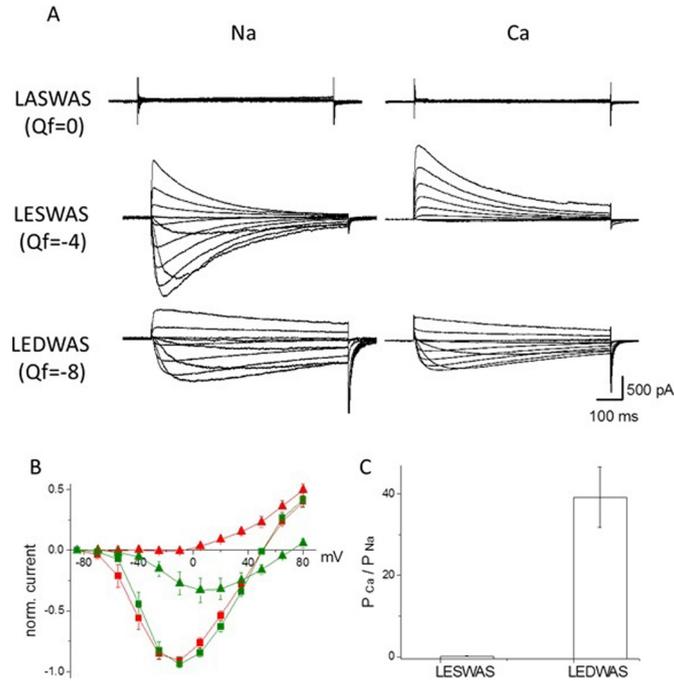
Fig. 5. Permeability to Na^+ and Ca^{2+} of the wild type NaChBac (LESWAS) ion channel and its mutants (LASWAS and LEDWAS). (A) Representative whole cell current vs. time records obtained for channels in bath solution containing 140 mM Na^+ (left) or 100 mM Ca^{2+} (right). (B) Current–voltage I–V relationships ($\pm$ SEM are shown as bars, $n = 6 - 12$)) for LESWAS in Na^+ solution (red squares) and Ca^{2+} solution (red triangles) and LEDWAS in Na^+ solution (green squares) and Ca^{2+} solution (green triangles) normalized to the maximal peak Na^+ current from the same cell. (C) Permeability Na^+/Ca^{2+} ratios determined using reversal potentials, as described in [30], indicate that LEDWAS is a Ca^{2+} selective channel.

The ICB model [12] *predicts* that blockade by Ca^{2+} (or any other strong blocker) can be described by the Langmuir isotherm:

$$X([Ca]) = \ln\left(\frac{J([Ca])}{J(0) - J([Ca])}\right) = \ln\left(\frac{1 - P_c^*}{P_c^*}\right)$$
$$= \ln(IC_{50}) - \ln([Ca]), \qquad (9)$$

where the monovalent partial current $J([Ca])$ as a function of the bulk concentration $[Ca]$) is described by a Fermi-Dirac function (4) that is equivalent to the Langmuir isotherm (9) and IC_{50} is the Ca^{2+} concentration for which $J(IC_{50}) = 0.5J(0)$. Note that (9) strictly predicts a logarithmic slope of unity, $s = dX/d\ln([Ca]) = 1$. A similar equation was derived in [19]. Equation (9) is also applicable to the drug-driven blockade of bacterial mutants [5].

Figure 4A demonstrates an absence of divalent blockade for LESWAS in marked contrast with the strong blockade for LEDWAS mutants, which is well-fitted by the Langmuir isotherm (9) with a threshold value $IC_{50} = 5\,\mu M$ ($s = 1 \pm 0.05$). The IC_{50} value can in principle be connected to Q_f [12] but it will require better knowledge of the SF dimensions and will be a target of future research.

Figure 4B shows the corresponding E_{rev} results to define the carrier type for different $[Ca]$ values. It shows that, for LEDWAS, E_{rev} at low $[Ca]$ values starts from the same 50 mV as LESWAS (using a 140 mM Na^+ bath) but, from the point where the current starts to increase with further growth of $[Ca]$ ($\approx$1 mM), it rises rapidly to 72 mV,

which is the value measured for a 100 mM Ca^{2+} bath (i.e., in the absence of extra cellular Na^+). This implies that, similarly to the L-type calcium channel, AMFE in the LEDWAS mutant involves the substitution of the sodium current by calcium one.

Taken together, the results described above provide some experimental validation of the ICB model. In particular, they confirm the importance of Q_f as a determinant of NaChBac ionic valence selectivity. Increasing the negative charge in the SF results in permeability for divalent cations and it leads to phenomena such as divalent blockade of the Na^+ current and AMFE. Moreover, the close fitting of the current decay by equation (9) confirms one of the main ICB results, viz. that the SF occupancy is described by a Fermi-Dirac distribution.

7 General ICB-based conduction vs. Q_f scheme

Figure 6 illustrates diagrammatically the quasi-periodic sequence of multi-ion blockade/conduction modes described by equation (6) with growth of $\{n\}$, where Q_f (and P_b) increase, together with putative identifications of particular modes and of the NaChBac mutants used in this work.

– The state Z_0 with $Q_f = 0$ represents the ICB blocked state for the empty selectivity filter, brought about by image forces – as observed experimentally in LASWAS (see above) and also in artificial nanopores [14].
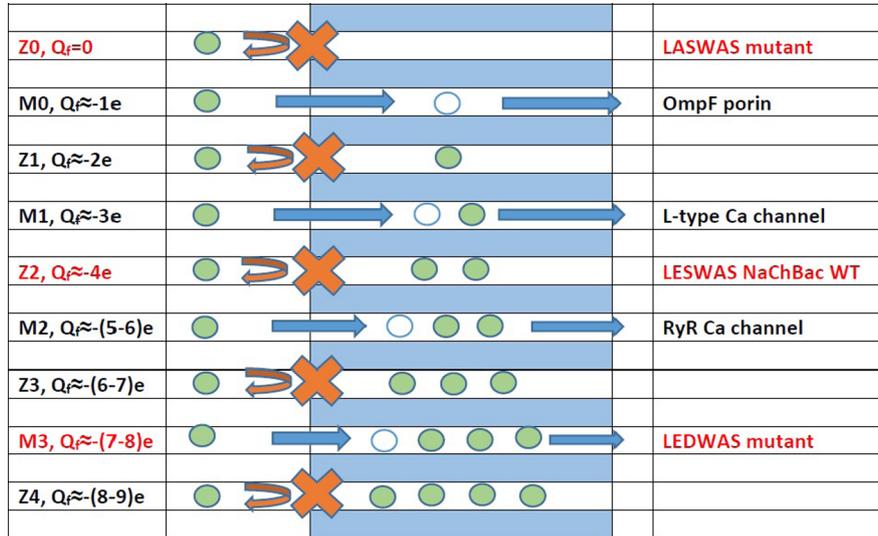
Fig. 6. Evolution of the Ca^{2+} conduction mechanism with increasing absolute value of effective fixed charge $|Q_f|$, showing the Coulomb blockade oscillations of multi-ion conduction/blockade states. The neutralized states Z_n providing blockade are interleaved with resonant conduction states M_n. The $|Q_f|$ value increases from top to bottom, as shown. Green circles indicate Ca^{2+} ions, unfilled circles show vacancies (virtual empty states during the knock-on process). The right-hand column indicates the preliminary identifications of particular channels/mutants corresponding to particular mechanisms. Mutants studied here are shown in red.

– The first resonant point M_0 corresponds to single-ion (i.e., $\{n\} = \frac{1}{2}$) barrier-less conduction, and can be related to the OmpF porin [11,35].
– This state is followed by the Z_1 blocked state, and then by the M_1 state describing double-ion knock-on and identified with L-type calcium channels [10].
– On a preliminary basis, the NaChBac wild type channel ($Q_f = -4e$) can be identified with the Z_2 blockade point, such an identification being supported by both BD simulations and patch-clamp studies.
– The three-ion resonance $M_2 = -(5-6)e$ can be identified with the RyR calcium channels [36].
– The calcium-selective $M_3 \approx -(7-8)e$ resonant point can be identified with the LEDWAS mutant having $Q_f = -8e$. Further research is needed to resolve the observed differences between the nominal and effective values of Q_f for LESWAS and LEDWAS (see also [37]).

bands. In particular we have shown that growth of Q_f from $-4e$ to $-8e$ leads to strong divalent blockade of the sodium current by micromolar concentrations of Ca^{2+} ions, similar to the effects seen in calcium channels. The onset of divalent blockade (shape of the current-concentration curve) follows the Langmuir isotherm, consistent with ICB model predictions.

8 Conclusions

We have reported the initial results of the first biological experiments undertaken to test the predictions of the ICB model of ion channel conduction. In particular, we used patch-clamp experiments to investigate Ca^{2+}/Na^+ conduction and selectivity, AMFE, and ionic concentration dependences in the bacterial NaChBac channel ($Q_f = -4e$) and in its charge-varied mutants with $Q_f = 0$ and $Q_f = -8e$. We compare the results with earlier Brownian dynamics simulations of the permeation process, and with theoretical predictions of the ICB model which we have extended to encompass bulk concentration affects.

We find that the ICB model provides a good account of both the experimental (AMFE and valence selectivity) and the simulated (discrete multi-ion conduction and occupancy band) phenomena observed in Ca^{2+} channels, including concentration-related shifts of conduction/occupancy

Appendix A: Generation, expression and measurements of NaChBac channels

NaChBac (GenBank accession number BAB05220 [38]) cDNA$^+$ was synthesised by EPOCH Life Science (www.epochlifescience.com) and subcloned into the mammalian cell expression vector pTracer-CMV2 (Invitrogen). Amino acid mutations in the pore region of NaChBac were introduced using the Q5® SDM Kit (New England BioLabs Inc.) in accordance with the manufacturers instructions. All mutations were confirmed by DNA$^+$ sequencing prior to transfection of Chinese Hamster Ovary (CHO) cells with TransIT-2020 (Mirus Bio). Transfected cells (expressing GFP) were identified with an inverted fluorescence microscope (Nikon TE2000-s) and their electrophysiological properties were determined 24–48 h after transfection.

Whole-cell currents were recorded using an Axopatch 200A (Molecular Devices, Inc., USA) amplifier. Patch clamp signals were digitized using Digidata1322 (Molecular Devices, Inc., USA) and filtered at 2 kHz. Patch-clamp electrodes were pulled from borosilicate glass (Kimax, Kimble Company, USA) and exhibited resistances of 2–3 MOhm. The shanks of the pipettes tip were coated with beeswax in order to reduce pipette capacitance. The pipette (intracellular) solution contained (in mM): 120 Cs-methanesulfonate, 20 Na-gluconate, 5 CsCl, 10 EGTA, and 20 HEPES, pH 7.4 (adjusted by CsOH). Giga-Ohm seals were obtained in the bath (external) solution containing (in mM): 140 Na-methanesulfonate, 5 CsCl, 10 HEPES and 10 glucose, pH 7.4 (adjusted by CsOH), in which Na-methanesulfonate then was subsequently replaced with Ca-methanesulfonate in order to vary Na^+ and Ca^{2+} solution content (see main text). We used methanesulfonate salts in solutions to diminish the influence of endogenous chloride channels. Solutions were filtered with a 0.22 mm filter before use. Osmolarity of all solutions was 280 mOsm (adjusted using sorbitol).

Current–voltage data were typically collected by recording responses to a consecutive series of step pulses from a holding potential of -100 mV at intervals of 15 mV beginning at $+95$ mV. The bath solution was grounded using a 3M KCl agar bridge. All experiments were conducted at room temperature.

References

1. B. Hille, *Ion Channels of Excitable Membranes*, 3rd edn. (Sinauer Associates, Sunderland, MA, 2001)
2. J. Zheng, M.C. Trudeau (eds.), *Handbook of Ion Channels* (CRC Press, Taylor & Francis Group, Boca Raton, FL, 2015)
3. B. Eisenberg, Physiology **28**, 28 (2013)
4. L.X. Yue, B. Navarro, D.J. Ren, A. Ramos, D.E. Clapham, J. Gen. Physiol. **120**, 845 (2002)
5. L. Tang, T.M.G. El-Din, T.M. Swanson, D.C. Pryde, T. Scheuer, N. Zheng, W.A. Catterall, Nature **537**, 117 (2016)
6. C.E. Naylor, C. Bagnéris, P.G. DeCaen, A. Sula, A. Scaglione, D.E. Clapham, B.A. Wallace, EMBO J. **35**, 820 (2016)
7. W.A. Catterall, G. Wisedchaisri, N. Zheng, Nature Chem. Biol. **13**, 455 (2017)
8. J. Payandeh, T.M.G. El-Din, T. Scheuer, N. Zheng, W.A. Catterall, Nature **486**, 135 (2012)
9. B. Corry, M. Thomas, J. Am. Chem. Soc. **134**, 1840 (2012)
10. I.K. Kaufman, D.G. Luchinsky, R. Tindjong, P.V.E. McClintock, R.S. Eisenberg, Phys. Biol. **10**, 026007 (2013)
11. I.K. Kaufman, D.G. Luchinsky, R. Tindjong, P.V.E. McClintock, R.S. Eisenberg, Phys. Rev. E **88**, 052712 (2013)
12. I.K. Kaufman, P.V.E. McClintock, R.S. Eisenberg, New J. Phys. **17**, 083021 (2015)
13. M. Krems, M. Di Ventra, J. Phys. Condens. Matter **25**, 065101 (2013)
14. J. Feng, K. Liu, M. Graf, D. Dumcenco, A. Kis, M. Di Ventra, A. Radenovic, Nature Mater. **15**, 850 (2016)
15. E. von Kitzing, Membrane proteins: structures, interactions and models, in *Proc. 25th Jerusalem Symposium on Quantum Chemistry and Biochemistry, Jerusalem, May 18–21, 1992* (1992)
16. R.S. Eisenberg, in *New Developments in Theoretical Studies of Proteins*, edited by R. Elber (World Scientific, Singapore, 1996), pp. 269–357
17. J. Zhang, A. Kamenev, B.I. Shklovskii, Phys. Rev. E **73**, 051205 (2006)
18. J.L. Liu, R. Eisenberg, J. Phys. Chem. B **117**, 12051 (2013)
19. J.L. Liu, B. Eisenberg, J. Chem. Phys. **141**, 075102 (2014)
20. C.W.J. Beenakker, Phys. Rev. B **44**, 1646 (1991)
21. W. Nonner, D.P. Chen, B. Eisenberg, Biophys. J. **74**, 2327 (1998)
22. B. Corry, T.W. Allen, S. Kuyucak, S.H. Chung, Biophys. J. **80**, 195 (2001)
23. C. Guardiani, P.M. Rodger, O.A. Fedorenko, S.K. Roberts, I.A. Khovanov, J. Chem. Theor. Comp. **13**, 1389 (2017)
24. B. Roux, T. Allen, S. Berneche, W. Im, Q. Rev. Biophys. **37**, 15 (2004)
25. W. Nonner, D. Gillespie, D. Henderson, B. Eisenberg, J. Phys. Chem. B **105**, 6427 (2001)
26. D. Krauss, B. Eisenberg, D. Gillespie, Eur. Biophys. J. **40**, 775 (2011)
27. P.H. Nelson, J. Chem. Phys. **134**, 165102 (2011)
28. D.G. Luchinsky, W.A.T. Gibby, I. Kaufman, D.A. Timucin, P.V.E. McClintock, arxiv:1604.05758 (2016)
29. J. Zhang, A. Kamenev, B.I. Shklovskii, Phys. Rev. E **73**, 051205 (2006)
30. Y.M. Sun, I. Favre, L. Schild, E. Moczydlowski, J. Gen. Physiol. **110**, 693 (1997)
31. I. Kaufman, W. Gibby, D. Luchinsky, P. McClintock, R. Eisenberg, in *Proc. 23rd Int. Conf. on Noise and Fluctuations (ICNF), Xian (IEEE Conf. Proc., 2015)* (2015), doi:10.1109/ICNF.2015.7288558.
32. P.G. DeCaen, Y. Takahashi, T.A. Krulwich, M. Ito, D.E. Clapham, eLife **3**, e04387 (2014)
33. W.A. Sather, E.W. McCleskey, Ann. Rev. Physiol. **65**, 133 (2003)
34. P.T. Ellinor, J. Yang, W.A. Sather, J.F. Zhang, R.W. Tsien, Neuron **15**, 1121 (1995)
35. H. Miedema, A. Meter-Arkema, J. Wierenga, J. Tang, B. Eisenberg, W. Nonner, H. Hektor, D. Gillespie, W. Meijberg, Biophys. J. **87**, 3137 (2004)
36. D. Gillespie, Biophys. J. **94**, 1169 (2008)
37. I.K. Kaufman, D.G. Luchinsky, W.A.T. Gibby, P.V.E. McClintock, R.S. Eisenberg, J. Stat. Mech. **2016**, 054027 (2016)
38. D.J. Ren, B. Navarro, H.X. Xu, L.X. Yue, Q. Shi, D.E. Clapham, Science **294**, 2372 (2001)